This is a preprint, the final version is subject to change, of the American Mineralogist (MSA)
Cite as Authors (Year) Title. American Mineralogist, in press.
DOI: https://doi.org/10.2138/am-2019-7079

Revision 1

A Cr^{3+} luminescence study of natural topaz $Al_2SiO_4(F,OH)_2$ up to 60 GPa

Earl F. O'Bannon III[1] and Quentin Williams[2]

[1]Physics Division, Physical & Life Sciences Directorate, Lawrence Livermore National Laboratory, Livermore, CA 94551, USA

[2]Department of Earth & Planetary Sciences, University of California Santa Cruz, CA 95064 USA

Abstract

Topaz [$Al_2SiO_4(F,OH)_2$] is a subduction-related mineral that is found in metasediments and has a large pressure and temperature stability field. Here, we use luminescence spectroscopy of Cr^{3+} to probe the Al site in topaz under high-pressure up to ~60 GPa, which corresponds to a depth of ~1400 km in the Earth. This technique allows us to probe all three unique Al environments (e.g. $[AlO_4(OH)_2]^{7-}$, $[AlO_4(F)_2]^{7-}$, and $[AlO_4OH,F]^{7-}$) simultaneously under high-pressure. We find that the R-line luminescence from all three Al environments shifts linearly to longer wavelength to ~ 40 GPa. Above ~40 GPa, they shift non-linearly and begin to flatten out at ~48 GPa, with a pressure shift of ~0 cm^{-1}/GPa from ~48-55 GPa. Our results combined with previous high-pressure single-crystal diffraction results to ~45 GPa strongly indicate that there is a change in the compression mechanism in topaz above ~40 GPa. Our high-pressure room temperature results show that topaz' metastable persistence on compression is among the most extreme among tetrahedrally-coordinated silicates.

Keywords: Topaz, High-pressure, Cr^{3+} luminescence, nesosilicates

Introduction

Metamorphic minerals transport water and volatiles to depth during subduction. The dehydration of minerals in subduction zones is well-known to cause partial melting and back arc volcanism. The water budget of a subducting slab is complex, but it is generally agreed that the amount of water subducted is substantially greater than the amount of water released above the back arc

(Peacock 1990; Poli and Schmidt 1995; Schmidt and Poli 1998; Williams and Hemley 2001). Minerals such as lawsonite [$CaAl_2Si_2O_7(OH)_2 \cdot H_2O$], phengite [$K(AlMg)_2(OH)_2(SiAl)_4O_{10}$], topaz [$Al_2SiO_4(F,OH)_2$], and other dense hydrous phases are thought to be able to transport water and volatiles to depths greater than ~150 km (Wunder et al. 1993; Pawley 1994; Schmidt and Poli 1994; Domanik and Holloway 1996; Ono 1998; 1999) .

Topaz [$Al_2SiO_4(F,OH)_2$] is a subduction-related mineral that is found in metasediments and has a large pressure and temperature stability field. Topaz can form in pelitic sediments in subduction zones at conditions starting near 5.0 GPa and ~600 °C. Topaz has been shown to be stable to at least 12 GPa and ~1100 °C (Holland et al. 1996). Hydroxyl rich topaz has also been found in high-pressure and ultra high-pressure belts of the Sulu terrane, China (Zhang et al. 2002). In order to fully understand H_2O and fluorine (F) cycling in subduction zones, detailed studies of the minerals that are likely to carry H_2O and F to depth are required. Previous high-pressure, room temperature spectroscopic investigations focused on looking at the pressure dependence of the OH stretches and silicate vibrations (Bradbury and Williams, 2003; Komatsu et al. 2005). Spectra were collected up to ~24 and ~30 GPa, respectively, and no phase transitions were observed. High-pressure room temperature single-crystal X-ray diffraction studies have also been reported up to ~45 GPa and, again, no phase transitions were observed (Komatsu et al. 2005; Gatta et al. 2006; Gatta et al. 2014). Moreover, Gatta et al. (2014) suggest that H-bonding in natural F-rich topaz likely strengthens in response to external pressure based on a *donor-acceptor* distance argument. Raman and infrared spectroscopic results reported by Bradbury and Williams (2003) and Komatsu et al. (2005) find that the H-bonding in F-rich topaz becomes weaker under pressure. Hence, there are ambiguities associated with the high-pressure response of natural F-rich topaz to pressure. More recently, using first principles techniques topaz-OH was investigated at high-pressure and two distinct spacegroups that are close in energy were found, orthorhombic *Pbnm* and monoclinic $P2_1/c$ (Mookherjee et al. 2016). Moreover, another first principles study investigated the effect of

fluorine content on the elastic behavior of topaz, and found that orthorhombic *Pbnm* symmetry was the lowest energy for F-topaz, but orthorhombic $Pbn2_1$ was relevant for intermediate F/OH compositions (Ulian and Valdre 2017).

The luminescence spectrum of topaz has primarily been studied at ambient pressure and various temperatures (Gaft et al. 2003; Tarashchan et al. 2006). In end-member F-topaz, there is one unique Al site (Figure 1); however, in partially hydroxylated topaz, there are three unique Al environments whose abundances depend on the relative concentrations of OH and F (e.g. $[AlO_4(OH)_2]^{7-}$, $[AlO_4(F)_2]^{7-}$, and $[AlO_4OH,F]^{7-}$). When trace amounts of Cr^{3+} are substituted into the lattice, these different environments give rise to three sets of overlapping transitions for each of the R_1 and R_2 fluorescence peaks. The two split components are produced by the transition from the doubly-split ^2E level to the $^4A_2$ ground state, and the three components of each of these peaks can be easily deconvolved. Here, we use luminescence spectroscopy of Cr^{3+} which substitutes into the Al sites as a probe of the octahedral site in partially hydroxylated topaz under high-pressure. Our experiments are oriented towards (1) determining if any phase transitions occur in topaz under compression, (2) measuring the pressure shift of the R-lines, and (3) determining if any changes in the compressional mechanisms of topaz occur at high pressures.

Experimental Methods

Our sample was a natural gem quality imperial topaz sample from Capao Topaz mine, Minas Gerais, Brazil. The sample identity was confirmed with Raman spectroscopy, luminescence spectroscopy, and single-crystal X-ray diffraction, all of which agree well with previous studies (Alston et al. 1928; Beny and Piriou 1987; Gaft et al. 2003; Tarashchan et al. 2006). Ambient single-crystal diffraction measurements were conducted at beamline 11.3.1 (Stan et al. 2018) at the Advanced Light Source at Lawrence Berkeley National Laboratory in Berkeley, California. Trace element concentrations of topaz were measured with a PhotonMachines Analyte 193H, which is a 193-nm ArF excimer laser system

coupled with a ThermoScientific ElementXR single-collect or magnetic sector ICP-MS. The instrument was calibrated with a SRM 610 trace element glass from NIST, and Al was used as the internal standard. The following trace elements were measured, Cr 145 ±68, V 35 ±14, Fe 68 ±43, Mn 2.0 ±0.4, and Ti is below detection limits (all numbers in ppm). From single-crystal diffraction experiments we obtain unit cell parameters of *a*= 4.6441(4), *b*= 8.8122(7), and *c*= 8.3596(6), and we refine a F occupancy 0.743 (±0.026), with the balance being hydroxyl ions, or approximately a 3:1 F/OH ratio.

High static pressures were generated using a symmetric type diamond anvil cell (DAC). Anvils were 16 sided type Ia diamonds with culet sizes that ranged from 500 to 200 µm depending on target pressure, and gaskets were made from rhenium or spring steel. Gaskets were preindented to ~ 30 µm thickness and a hole was drilled that was ~ 2/3 the diameter of the diamond culet that was used. Samples were ~25 x 20 x 10 µm in dimensions (LxWxH). The pressure medium was either 16:3:1 methanol:ethanol:water, Ne, or He depending on experimental pressure ranges. Ne and He gasses were loaded with a high pressure gas loading apparatus at the Advanced Light Source, Berkeley, CA. A single crystal of the sample along with at least two ruby spheres (Chervin et al. 2001) that were < 10 µm in diameter were loaded into the sample compartment. Pressures were determined using the standard ruby fluorescence pressure gauge (Dewaele et al. 2008) and data were collected on both compression and decompression.

Luminescence spectra were collected from 650-800 nm (15380-12500 cm^{-1}) with a Horiba LabRAM HR Evolution Raman spectrometer with a spectrometer focal length of 800 mm. Spectra were collected to a pressure of ~60 GPa and on decompression at 300 K using an excitation wavelength of 532 nm. An Olympus BXFM-ILHS microscope with a 50x long working distance objective was used to focus the laser beam onto the sample. An 1800 lines/mm grating with a corresponding spectral resolution of ~1 cm^{-1} (or, equivalently, ~0.05 nm) was utilized. Combinations of Gaussian and Lorentzian functions were fit to the luminescence spectra with Horiba Labspec6 software.

Results and discussion

Emission band assignments

The luminescence spectra of topaz at various temperatures are shown in Figure 2. These spectra agree well with the previous studies of Gaft et al. (2003) and Tarashchan et al. (2006). At room temperature and pressure, the sharp R-line emissions, a broad $^4T_2$-$^4A_2$ transition, and vibrational sidebands are observed. At 77 K, the sharp R-lines shft to slightly shorter wavelength, and the $^4T_2$-$^4A_2$ transition becomes unresolvable. This assignment and observation agrees well with the ambient pressure spectra and the interpretation of Tarashchan et al. (2006). The three components of each R-line are easily observed at 77K, as well as a more complex set of lines associated with emission from neighboring Cr^{3+}-ions (N-lines).

Figure 3 shows a representative deconvolution of the R-lines at room pressure and temperature. Three emission bands can be fit under each R-line. Considering the O4 site is 74(3)% occupied by F, the majority of the Al sites in this topaz have the $[AlO_4(F)_2]^{7-}$ environment, with the mixed site ($[AlO_4OH,F]^{7-}$) being the next most abundant, and the $[AlO_4(OH)_2]^{7-}$ environment being the least abundant. Hence, we assign the intense 683.5 nm R_1 band to the $[AlO_4(F)_2]^{7-}$ site, the 684.7 nm R_1 band to the $[AlO_4OH,F]^{7-}$ site, and the 683.1 nm R1 band to the $[AlO_4(OH)_2]^{7-}$ site.

High-pressure spectra

Representative high-pressure luminescence spectra of the topaz R-lines up to ~55.0 GPa are shown in Figure 4. As with all Cr^{3+} R-line emissions in oxides observed to date (Kottke and Williams 1983; Dolan et al. 1986; Wamsley and Bray 1994; O'Bannon and Williams 2016; 2017; O'Bannon et al. 2018), the R-lines shift to longer wavelength under compression to ~55.0 GPa. The intensity of the R-lines decreases as a function of pressure, and they become unresolvable above ~55 GPa (they continued to be unresolvable to at least 60 GPa). On decompression from 60 GPa, the R-lines again became

resolvable near 55 GPa, and no hysteresis of the luminescence peaks was observed. The loss of intensity above 55 GPa is probably due to pressure-induced migration of the absorption bands in topaz to wavelengths such that pumping these transitions with 532 nm excitation becomes inefficient.

The pressure shifts of the R-lines of topaz are plotted in Figure 5, and they are tabulated in Table 1. The R-lines are labeled in accord with their intensity. The most intense components (associated with a fully fluorinated environment) are R_1 and R_2, the intermediate intensity components are R_1' and R_2' (the mixed F/OH environment), and the least intense components are labeled R_1'' and R_2'' (the solely OH-bearing octahedra). The pressure shifts of the R-lines are remarkably linear below ~40 GPa suggesting that the compaction mechanism of topaz, as manifested by shifts in bonding/electron density at the Al site, remains constant up to ~40 GPa. Above 40 GPa the pressure shifts become non-linear suggesting that the compressional mechanism changes above this pressure. This apparent shift in compressional mechanism is not concordant with the constant compressional mechanism reported based on single crystal results by Gatta et al. (2014). As a side note, such a marked decrease in the pressure dependence of the R-lines is without precedent. The luminescence of Cr^{3+} in three other geologic oxides has been probed in to the pressure range in which we examine topaz: ruby, alexandrite and tourmaline. No such slope change in the pressure shift of the ruby R-lines is observed up to at least 156 GPa at room temperature (Eggert et al. 1988), and the structure of ruby does not undergo any phase transitions up to at least 176 GPa at room temperature (Jephcoat et al. 1989). Similarly, the R-lines in alexandrite ($BeAl_2O_4$) shift monotonically up to at least 50 GPa (Jahren et al. 1991), as do the emission bands of dravite-tourmaline to 65 GPa (O'Bannon et al. 2018: in this case, a modest splitting occurs associated with the loss of a mirror plane at 15 GPa). This suggests that the compression mechanisms of ruby, alexandrite and tourmaline do not change up to at least 176 GPa, 50 GPa and 65 GPa, respectively, and indeed no notable change in the compression mechanism of any of these phases has been reported, and the R-lines in each phase show no marked shifts in slope.

Gatta et al. (2014) report that neither phase transitions, changes in compressional mechanism, nor changes in Al-site distortion are observed under compression to ~45 GPa. However, the data from their study show that the pressure dependence of the Al-site volume is essentially constant above ~40 GPa (Figure 6a). The Si site volumes and bond lengths reported by Gatta et al. (2014) above ~40 GPa are a bit more scattered than those of the Al site, and do not clearly show a trend (Figure 7). The individual Al-O/F bond lengths as a function of pressure show similar behavior, with the Al-O bond lengths becoming nearly constant above about ~40 GPa (Figure 6b); the Al-F bond lengths may show similar behavior, but they are sufficiently scattered that it is difficult to conclusively resolve a trend. Notably, these changes in Al-site volume and Al-O/F bond distances were not discussed in detail by Gatta et al. (2014) since in the context of their entire data set, these deviations are not statistically significant, and they thus were likely cautious when interpreting their results. However, our fluorescence experiments were conducted using both He and Ne pressure media (Figure 5) in order to rule out the possibility that non-hydrostaticity in Ne at pressures above 40 GPa impacted our measurements. Thus, it is possible that the previous single-crystal study of Gatta et al. (2014) also observed the beginning of the change in compression mechanism that we identify using luminescence spectroscopy.

Given the unusual behavior of the luminescence of topaz above 40 GPa, a short assessment of the degree of nonhydrostaticity in the samples is likely of value. Clearly, from the luminescence behavior of ruby, alexandrite and tourmaline to pressures above 50 GPa (Eggert et al. 1988; Jahren et al. 1991; O'Bannon et al. 2018), non-hydrostaticity itself does not typically produce anomalous behavior of Cr^{3+}-luminescence at extreme conditions. In terms of quantifying stress gradients, Klotz et al. (2009) report that the standard deviation in pressure in a He pressure medium at ~40 GPa is ~0.2 GPa, and the more quantitative study of Takemura and Dewaele (2008) report that the uniaxial stress component of an Au sample in a He pressure medium at ~ 40 GPa is 0.11 GPa. Might these small differential stresses generate the change in R-line slope above 40 GPa? If the pressure dependence of the topaz R-lines is,

through some mechanism, altered by nonhydrostatic conditions (alone among oxides probed to these pressures to date) induced by the chosen pressure media, then we would anticipate that different levels of nonhydrostaticity should induce different onset pressures of the anomalous behavior. As the standard deviation in pressure and the uniaxial stress component in a Ne pressure medium is known to be larger than in He (e.g., Klotz et al. 2009), then we would expect that the onset pressure of the change in pressure dependence of the topaz R-lines would be at lower pressures in a Ne medium versus a He medium. However, Figure 5 shows that the change in pressure dependence of the Topaz R-lines occurs at essentially the same pressure in both the He and Ne medium experiments. Thus, the change we observe is likely an intrinsic phenomenon generated by compaction of topaz, and does not appear to be correlated with non-hydrostatic effects.

R-line separation and FWHM

The separation between the R_1 and R_2 bands of all three components of the R-lines increases as a function of pressure. Figure 8 shows the separation of the three components of the R-lines. All three components behave in a similar way and their separation increases as pressure increases; again, this behavior is fully reversible on decompression. As this separation arises from the distortion of the Al/Cr-octahedron from an ideal geometry (e.g., Syassen, 2008), this increase in separation implies that the Al-sites become more distorted under compression. Indeed, the calculated quadratic elongation for the Al site reported by Gatta et al. (2014) shows that the Al site becomes more distorted under compression to 45 GPa. This distortion, as derived from luminescence spectroscopy, represents a measure of the distortion of the site away from ideal octahedral symmetry, and as such is a conflation of internal octahedral deformation such as (1) cation off-centeredness, (2) deviation of the anion configuration from octahedral symmetry, and (3) shifts in charge distribution induced by having both F and O as part of the octahedra. The observed decrease in the R-line separation of the R_1'' and R_2'' components above 40 GPa is likely due to the difficulties in fitting the weak R_1'' component because of peak broadening and

low intensity of the emission bands at the highest pressure of these experiments. There is also a change in slope above ~40 GPa in R_1-R_2 and R_1'-R_2' (Figure 8b and 8c) which is consistent with a change in deformation mechanism, as indicated by both the R-line pressure dependences and single crystal diffraction data (Figures 5 and 6). It is possible that the deviation from the lower pressure trend of the R-line separation above 40 GPa is largest for the doubly hydroxylated site, intermediate in magnitude for the singly hydroxylated site, and smallest for the fully fluorinated site (Figure 8).

Full widths at half maximum (FWHM) of the topaz R-lines as a function of pressure are shown in Figure 9. The peak width of the R-lines increases as pressure increases. Notably, at the highest pressures, the peakwidth with a He medium is narrower than the peakwidth in Ne, which shows that, unsurprisingly, the He experiment is more hydrostatic than the Ne experiment. This agrees well with previously reported results on differential stress in different pressure media (Klotz et al. 2009). As with the shift in R_1-R_2 separation, the uniform increase in peakwidth as a function of pressure are consistent with the Al-sites becoming more distorted with pressure, although non-hydrostatic stress (even within He) is likely to also play a role in this broadening.

It should be noted that Gatta et al. (2014) modeled their structures as fully fluorinated, although the reported composition of their sample was $[Al_{2.00}Si_{1.05}O_{4.00}(OH_{0.26}F_{1.75})]$. In high-pressure single-crystal diffraction, it is sometimes necessary to simplify the structural model. In the case of topaz, modeling it as fully fluorinated is a reasonable simplification since the electron density of a bonded F and O atom are difficult to resolve within a typical high-pressure single-crystal dataset. So, the structural model of Gatta et al. (2014) is not expected to fully capture subtle differences in the compressional behavior of the three unique Al environments since their structures reflect an average change of the Al-F/OH bond length. Cr^{3+} luminescence allows us to probe all three Al environments under compression and demonstrates the sensitivity of this technique to different environments. The pressure shift, R-line

separation, and FWHM of the Cr^{3+} luminescence bands all behave slightly differently from one another, indicating that each Al environment responds differently to compression. Gatta et al. (2014) report that compression of topaz is mainly accommodated by contraction of the polyhedral bond distance, along with polyhedral tilting. As shown in Figure 6b, Gatta et al. (2014) report two populations of bonds in the Al-site, with the Al-O bonds being more compressible than the Al-F bonds. Moreover, the pressure dependences of the Al-O and Al-F bond lengths reported by Gatta et al. (2014) change above ~40 GPa. This change in behavior could be correlated with changes in H···H repulsive effects and/or in the H-bonding environment of the hydroxyls. Ulian and Valdre (2017) report in their density functional theoretical study of topazes with different F/OH ratios that complex H-bonding environments (bifurcated and trifurcated H-bonds) are established under compression. Moreover, our luminescence data suggest that the hydroxylated and the mixed F/OH sites show the largest changes above ~40 GPa (Figure 8a and 8c). Hence, a shift to a compressional mechanism where polyhedral tilting becomes the dominant compaction mechanism (with a possible additional role associated with tetrahedral deformation: Figure 7), with bond contraction of the Al-polyhedra ceasing to play a significant role likely occurs above ~40 GPa. This shift is likely associated with changes in H-bonding. Whether the exhaustion of octahedral bond contraction as a compressional mechanism represents precursory behavior to a higher pressure phase transition remains unclear.

Implications

Our results suggest that the compressional mechanism of topaz changes above ~40 GPa; this shift is supported by the single crystal data reported by Gatta et al. (2014), but its presence was not previously recognized. The following discussion assumes that the Cr sites that our techniques has probed reflect the bulk high-pressure behavior of the octahedral sites in topaz which is a reasonable assumption given the relatively simple topology of the topaz structure and the relatively low concentration of Cr and other elemental substituents. Thus, it seems unlikely that the Al sites would

behave dramatically different from the Cr sites that our technique probes. The R-line splittings and FWHM of the luminescence bands are both consistent with the Al-sites in topaz becoming more distorted under compression up to 40 GPa (which is consistent with the high-pressure single-crystal results of Gatta et al. 2014). Our results also show that the high-pressure behavior of the different Al environments (e.g. $[AlO_4(OH)_2]^{7-}$, $[AlO_4(F)_2]^{7-}$, and $[AlO_4OH,F]^{7-}$) are similar to one another up to 40 GPa, suggesting that these different Al environments are notably close in their energetic stabilities a result that has not been previously reported. The behavior of the emission bands above 40 GPa suggests that the Al-polyhedra become less compressible above this pressure, and that polyhedral tilting and/or tetrahedral distortion may play more major roles in the compaction of topaz above this pressure than contraction of the Al-octahedra does. This shift is likely associated with changes in the H-bonding environment of the fully hydroxylated Al-sites and the mixed OH/F Al sites.

Thus, this change in slope of the R-lines above ~40 GPa, and associated shift in compressional mechanism, could represent precursory behavior to a phase transition. The observation that the luminescence spectra are fully reversible following compression to 60 GPa implies that any transition is either fully reversible, or occurs above 60 GPa at 300 K. A notable aspect is that topaz is, at 300 K, one of the most metastable tetrahedrally-coordinated silicates under compression known: for comparison magnesian olivine persists to 54 GPa prior to amorphizing (Santamaria-Perez et al. 2016). This stability is plausibly a consequence of (as with olivine) its tetrahedra being surrounded by stable, highly coordinated cations in a relatively simple arrangement (Figure 1) in which compression is dominantly achieved (initially) by simple polyhedral compaction. Similarly, diopside $[CaMgSi_2O_6]$ is a mineral that persists metastably at 300 K to very high pressures (Chopelas and Serghiou 2002; Plonka et al. 2012). Diopside undergoes a phase transition near 55 GPa where half of the Si-sites change coordination from SiO_4 to SiO_6 (Chopelas and Serghiou 2002; Plonka et al. 2012). However, unlike topaz and olivine,

diopside is a chain silicate and the topology of the structure allows for nearly diffusion-less coordination changes to occur in the Si sites at high-pressure.

If topaz does undergo a phase transition at a pressure above ~60 GPa, this pressure corresponds to a depth of >1400 km in the Earth. Even in cold subduction zones, topaz would probably be close to being in thermal equilibrium with the surrounding mantle at these depths (as it should predominantly form near the top of the slab, in pelitic sediments). Thus, no low temperature transition in topaz is likely to occur within Earth's interior, and the major transformations undergone by topaz are likely to be either dehydration or conversion to high pressure hydrous aluminous phases (Ono, 1999; Dobrzhinetskaya and Green, 2007). Nevertheless, the high degree of metastability exhibited by topaz at 300 K indicates that it could be a strong candidate to kinetically persist substantially beyond its stability field if present in lower temperature subduction zone environments.

Acknowledgments

We thank Rob Franks for assistance with the LA-ICPMS measurements, Dan Sampson for technical assistance with the Raman spectrometer detector, and Nico Giordano (CSEC U. Edinburgh) and Christine Beavers for assistance with data collection on beamline 11.3.1 and helpful discussions. A portion of this work was performed under the auspices of the US Department of Energy by Lawrence Livermore National Laboratory under Contract No. DE-AC52-07NA27344. Work partially supported by NSF through EAR-1620423 and COMPRES through NSF Cooperative Agreement EAR-1606856. This research used resources of the Advanced Light Source (beamline 11.3.1, now beamline 12.2.1) at Lawrence Berkeley Laboratory which is a DOE Office of Science User facility under Contract No. DE-AC02-05CH11231.

References

Alston, N. A., West, J., & Fellow, J. H. (1928). The structure of topaz $Al(F,OH)_2SiO_4$. *Proceedings of the Royal Society of London Series a-Containing Papers of a Mathematical and Physical Character*, 121, 358-367.

Beny, J. M., & Piriou, B. (1987). Vibrational-spectra of single-crystal topaz. *Physics and Chemistry of Minerals*, 15, 148-154.

Bradbury, S. E., & Williams, Q. (2003). Contrasting bonding behavior of two hydroxyl-bearing metamorphic minerals under pressure: Clinozoisite and topaz. *American Mineralogist*, 88, 1460-1470.

Chervin, J. C., Canny, B., & Mancinelli, M. (2001). Ruby-spheres as pressure gauge for optically transparent high pressure cells. *High Pressure Research*, 21, 305-315.

Chopelas, A., & Serghiou, G. (2002). Spectroscopic evidence for pressure-induced phase transitions in diopside. *Physics and Chemistry of Minerals*, 29, 403-408.

Dewaele, A., Torrent, M., Loubeyre, P., & Mezouar, M. (2008). Compression curves of transition metals in the Mbar range: Experiments and projector augmented-wave calculations. *Physical Review B*, 78, 104102.

Dobrzhinetskaya, L. F., & Green, H. W. (2007). Experimental studies of mineralogical assemblages of metasedimentary rocks at Earth's mantle transition zone conditions. *Journal of Metamorphic Geology*, 25, 83-96.

Dolan, J. F., Kappers, L. A., & Bartram, R. H. (1986). Pressure and temperature-dependence of chromium photoluminescence in $K_2NaGaF_6:Cr^{3+}$. *Physical Review B*, 33, 7339-7341.

Domanik, K. J., & Holloway, J. R. (1996). The stability and composition of phengitic muscovite and associated phases from 5.5 to 11 GPa: Implications for deeply subducted sediments. *Geochimica Et Cosmochimica Acta*, 60, 4133-4150.

Eggert, J. H., Goettel, K. A., & Silvera, I. F. (1989). Ruby at high pressure. I. Optical line shifts to 156 GPa. *Physical Review B*, *40*(8), 5724.

Gaft, M., Nagli, L., Reisfeld, R., Panczer, G., & Brestel, M. (2003). Time-resolved luminescence of Cr^{3+} in topaz $Al_2SiO_4(OH,F)_2$. *Journal of Luminescence*, 102, 349-356.

Gatta, G. D., Morgenroth, W., Dera, P., Petitgirard, S., & Liermann, H. P. (2014). Elastic behavior and pressure-induced structure evolution of topaz up to 45 GPa. *Physics and Chemistry of Minerals*, 41, 569-577.

Gatta, G. D., Nestola, F., & Ballaran, T. B. (2006). Elastic behaviour and structural evolution of topaz at high pressure. *Physics and Chemistry of Minerals*, 33, 235-242.

Holland, T. J. B., Redfern, S. A. T., & Pawley, A. R. (1996). Volume behavior of hydrous minerals at high pressure and temperature .2. Compressibilities of lawsonite, zoisite, clinozoisite, and epidote. *American Mineralogist*, 81, 341-348.

Jahren, A.H., Kruger, M.B., & Jeanloz, R. (1991) Alexandrite as a high-temperature pressure calibrant, and implications for the ruby fluorescence scale. *Journal of Applied Physics*, 71*,* 1579-1582.

Jephcoat, A. P., Hemley, R. J., & Mao, H. K. (1988). X-ray diffraction of ruby (Al_2O_3: Cr^{3+}) to 175 GPa. *Physica B+ C*, 150(1-2), 115-121.

Klotz, S., Chervin, J. C., Munsch, P., & Le Marchand, G. (2009). Hydrostatic limits of 11 pressure transmitting media. *Journal of Physics D-Applied Physics*, 42, 075413.

Komatsu, K., Kagi, H., Okada, T., Kuribayashi, T., Parise, J. B., & Kudoh, Y. (2005). Pressure dependence of the OH-stretching mode in F-rich natural topaz and topaz-OH. *American Mineralogist*, 90, 266-270.

Kottke, T., & Williams, F. (1983). Pressure-dependence of the alexandrite emission spectrum. *Physical Review B*, 28, 1923-1927.

Mookherjee, M., Tsuchiya, J., & Hariharan, A. (2016). Crystal structure, equation of state, and elasticity of hydrous aluminosilicate phase, topaz-OH ($Al_2SiO_4(OH)_2$) at high pressures. *Physics of the Earth and Planetary Interiors*, 251, 24-35.

O'Bannon, E. F., Beavers, C. M., Kunz, M., & Williams, Q. (2018). High-pressure study of dravite tourmaline: Insights into the accommodating nature of the tourmaline structure. *American Mineralogist*, 103, 1622-1633.

O'Bannon, E. F., & Williams, Q. (2016). Beryl-II, a high-pressure phase of beryl: Raman and luminescence spectroscopy to 16.4 GPa. *Physics and Chemistry of Minerals*, 43, 671-687.

O'Bannon, E. F., & Williams, Q. (2017). Delocalization in Cr^{3+} luminescence of clinochlore: A pressure-induced transition from single-ion emission to pair emission. *Journal of Physics and Chemistry of Solids*, 109, 89-99.

Ono, S. (1998). Stability limits of hydrous minerals in sediment and mid-ocean ridge basalt compositions: Implications for water transport in subduction zones. *Journal of Geophysical Research-Solid Earth*, 103, 18253-18267.

Ono, S. (1999). High temperature stability limit of phase egg, $AlSiO_3(OH)$. *Contributions to Mineralogy and Petrology*, 137, 83-89. Pawley, A. R. (1994). The pressure and temperature stability limits of lawsonite: Implications for H_2O recycling in subduction zones. *Contributions to Mineralogy and Petrology*, 118, 99-108.

Peacock, S. M. (1990). Fluid processes in subduction zones. *Science*, 248, 329-337.

Plonka, A. M., Dera, P., Irmen, P., Rivers, M. L., Ehm, L., & Parise, J. B. (2012). beta-diopside, a new ultrahigh-pressure polymorph of $CaMgSi_2O_6$ with six-coordinated silicon. *Geophysical Research Letters*, 39.

Poli, S., & Schmidt, M. W. (1995). H_2O transport and release in subduction zones: Experimental constraints on basaltic and andesitic systems. *Journal of Geophysical Research-Solid Earth*, 100, 22299-22314.

Santamaria-Perez, D., Thomson, A., Segura, A., Pellicer-Torres, J., Manjon, F. J., Cora, F., et al. (2016). Metastable structural transformations and pressure-induced amorphization in natural $(Mg,Fe)_2SiO_4$ olivine under static compression: A Raman spectroscopic study. *American Mineralogist*, 101, 1642-1650.

Schmidt, M. W., & Poli, S. (1994). The stability of lawsonite and zoisite at high-pressures: Experiments in CASH to 92 kbar and implications for the presence of hydrous phases in subducted lithosphere. *Earth and Planetary Science Letters*, 124, 105-118.

Schmidt, M. W., & Poli, S. (1998). Experimentally based water budgets for dehydrating slabs and consequences for arc magma generation. *Earth and Planetary Science Letters*, 163, 361-379.

Stan, C. V., Beavers, C. M., Kunz, M., & Tamura, N. (2018). X-Ray Diffraction under Extreme Conditions at the Advanced Light Source. *Quantum Beam Science*, 2, 4, 33 pp.

Syassen, K. (2008). Ruby under pressure. *High Pressure Research*, 28(2), 75-126.

Takemura, K., & Dewaele, A. (2008). Isothermal equation of state for gold with a He-pressure medium. *Physical review B*, *78*(10), 104119.

Tarashchan, A. N., Taran, M. N., Rager, H., & Iwanuch, W. (2006). Luminescence spectroscopic study of Cr^{3+} in Brazilian topazes from Ouro Preto. *Physics and Chemistry of Minerals*, 32, 679-690.

Ulian, G., & Valdre, G. (2017). Effects of fluorine content on the elastic behavior of topaz $Al_2SiO_4(F,OH)_2$. *American Mineralogist*, 102, 347-356.

Wamsley, P. R., & Bray, K. L. (1994). High-pressure optical studies of doped YAG. *Journal of Luminescence*, 60-1, 188-191.

Williams, Q., & Hemley, R. J. (2001). Hydrogen in the deep earth. *Annual Review of Earth and Planetary Sciences*, 29, 365-418.

Wunder, B., Medenbach, O., Krause, W., & Schreyer, W. (1993). Synthesis, properties and stability of $Al_3Si_2O_7(OH)_3$ (PHASE Pi), A hydrous high-pressure phase in the system Al_2O_3 - SiO_2 - H_2O (ASH). *European Journal of Mineralogy*, 5, 637-649.

Zhang, R. Y., Liou, J. G., & Shu, J. F. (2002). Hydroxyl-rich topaz in high-pressure and ultrahigh-pressure kyanite quartzites, with retrograde woodhouseite, from the Sulu terrane, eastern China. *American Mineralogist*, 87, 445-453.

Figure 1. Crystal structure of topaz looking along the *a*-axis. Crystal structure based on our own synchrotron X-ray structure refinement. Diagram generated in CrystalMaker ® v 8.7.6.

Figure 2. Cr^{3+} luminescence emission spectra of topaz at various temperatures. Inset shows a detailed view of the R-lines at 77 K showing the multi-component character of each R-line.

Figure 3. Deconvolution of the R-lines in topaz showing the three components of each R-line, at room pressure and temperature.

Figure 4. Representative high-pressure luminescence spectra of topaz up to ~55.0 GPa. Spectra were collected in a Ne pressure medium.

Figure 5. Pressure shift of the R-lines in topaz, triangles are in a 16:3:1 alcohol mix, circles are in He, and squares are in Ne. Error bars are smaller than the symbols.

Figure 6. Single crystal data on topaz from Gatta et al. (2014). Note both the (a) Al-site volume behavior above ~40 GPa and the (b) Al-O bond length behavior above ~40 GPa.

Figure 7. Single crystal data on topaz from Gatta et al. (2014). (a) Si-site volume and the (b) Si-O bond length.

Figure 8. R-line separation as a function of pressure (a) R_1''-R_2'' hydroxylated site (b) R_1-R_2 fluorinated site and (c) R_1'-R_2' F,OH site. Error bars are smaller than the symbols, and different pressure media are shown with the same symbols and colors as Figure 4.5.

Figure 9. Full width at half maximum of (a) R_1 and (b) R_2. The other components of the R-lines show similar trends but are not plotted for clarity.

Table 1. Pressure shift of each component of the R-lines for all three experiments. Notably, the pressure shifts between the Ne and He experiments are essentially identical. The larger errors from the He and Ne experiments are produced by the uncertainty in deconvolving all three components of the peaks in weaker, broader bands at higher pressures.

Assignment	Pressure shift (nm/GPa)	R^2 value
Ne experiment (up to 40 GPa)		
R_1''	0.27 ±0.10	0.997
R_1	0.29 ±0.10	0.997
R_1'	0.30 ±0.16	0.993
R_2''	0.18 ±0.08	0.998
R_2	0.20 ±0.06	0.999
R_2'	0.22 ±0.08	0.998
He experiment (up to 40 GPa)		
R_1''	0.27 ±0.11	0.998
R_1	0.28 ±0.07	0.999
R_1'	0.31 ±0.14	0.998
R_2''	0.19 ±0.14	0.994
R_2	0.20 ±0.10	0.997
R_2'	0.22 ±0.13	0.996
16:3:1 experiment (up to 15 GPa)		
R_1''	0.29 ±0.01	0.998
R_1	0.29 ±0.01	0.998
R_1'	0.32 ±0.01	0.998
R_2''	0.22 ±0.01	0.998
R_2	0.22 ±0.01	0.998
R_2'	0.26 ±0.01	0.998

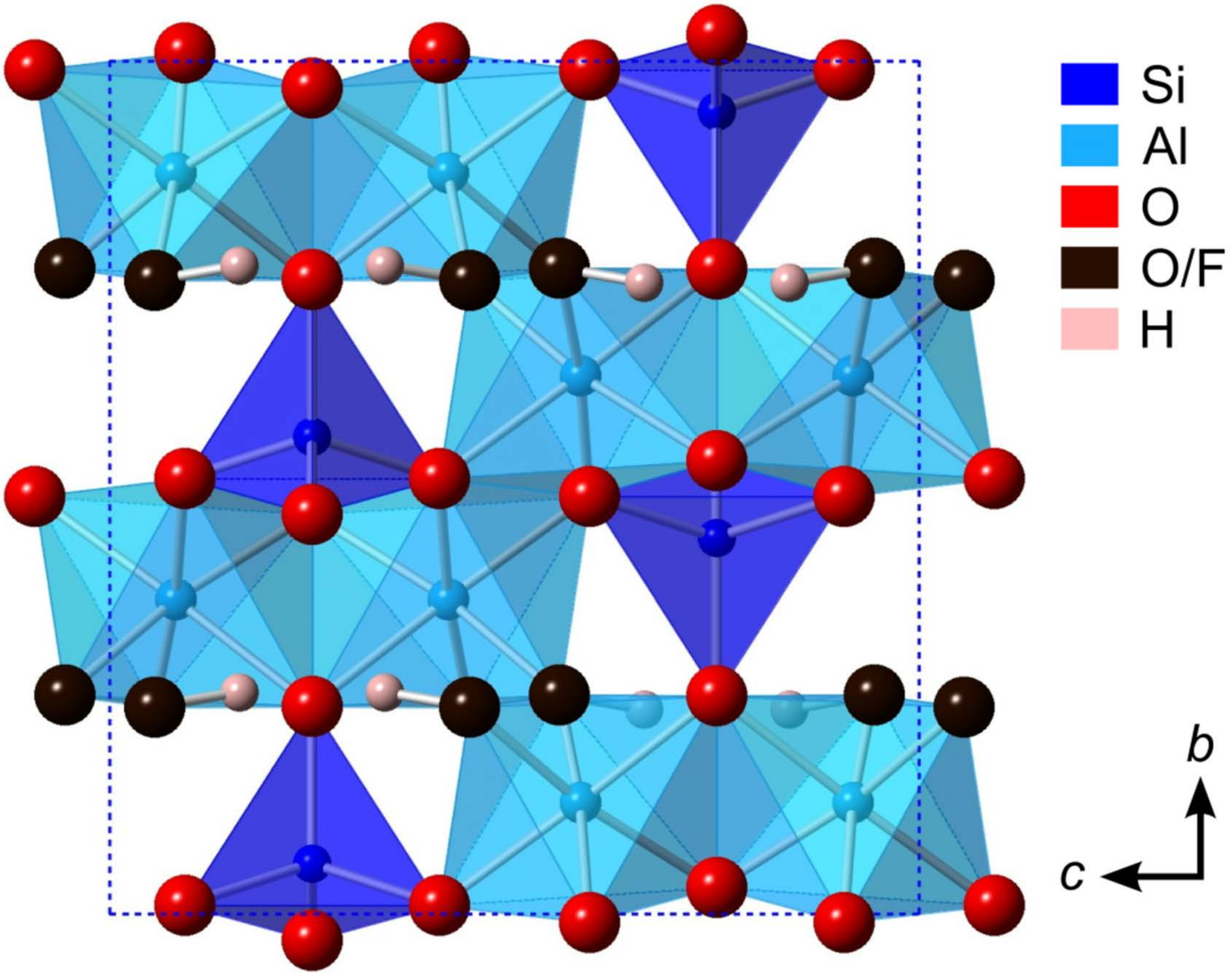

Figure 1

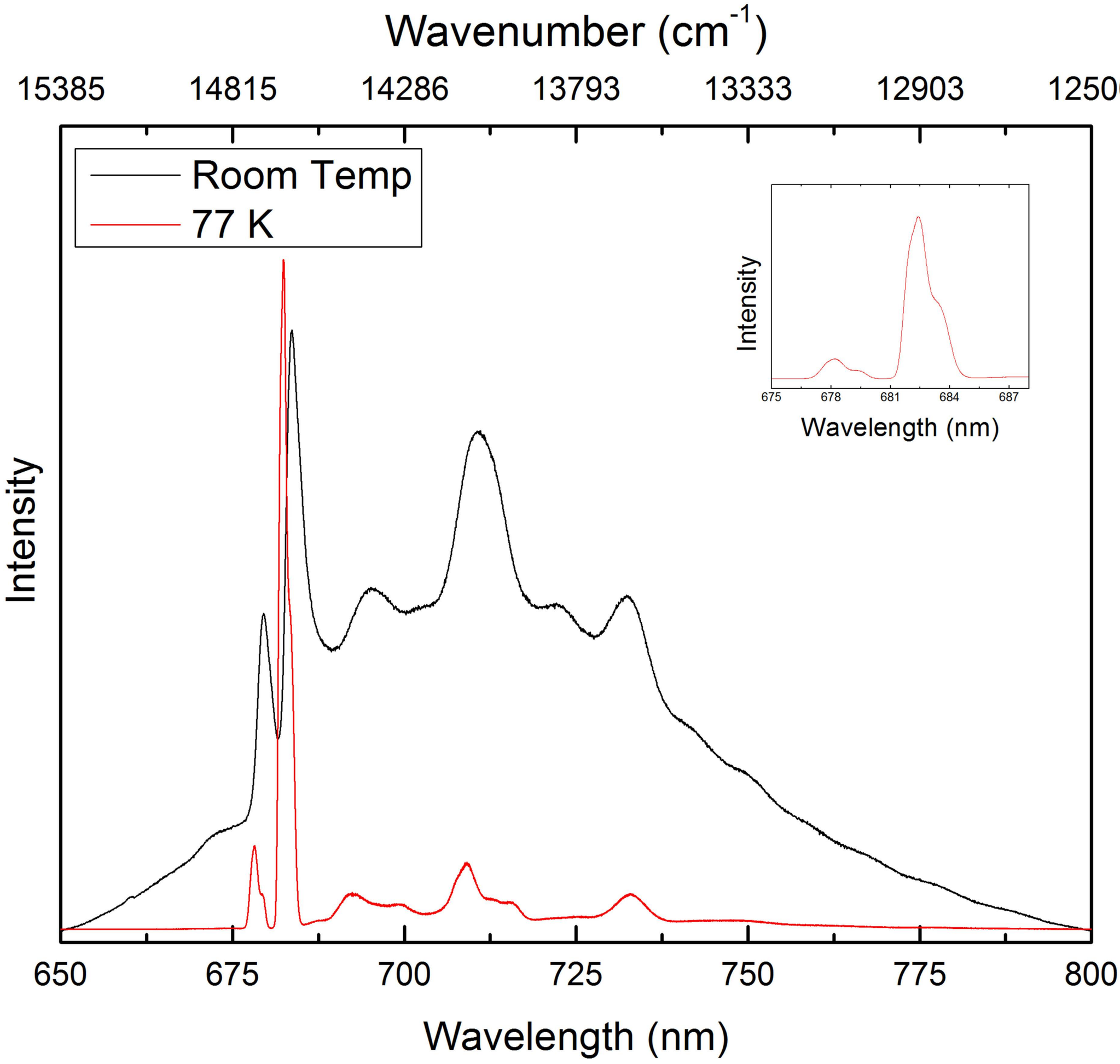
Wavenumber (cm-1)
15385
14815
14286
13793
13333
12903
12500
Room Temp
77 K
Intensity
650
675
700
725
750
775
800
Wavelength (nm)
Intensity
675
678
681
684
687
Wavelength (nm)

Figure 2

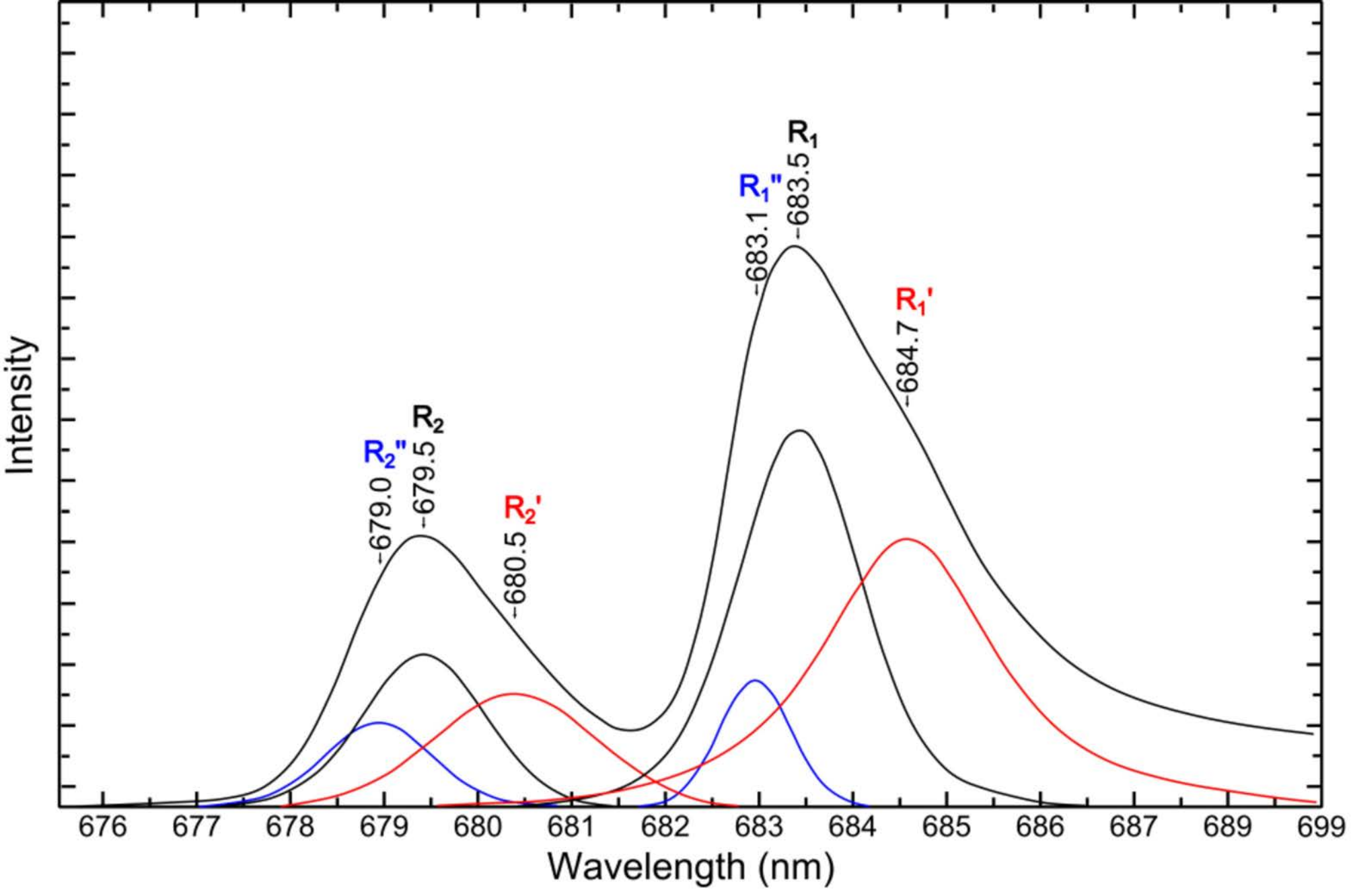
Intensity
Wavelength (nm)
676
677
678
679
680
681
682
683
684
685
686
687
689
699
R1
R1"
R1'
R2
R2"
R2'
683.5
683.1
684.7
679.5
679.0
680.5

Figure 3

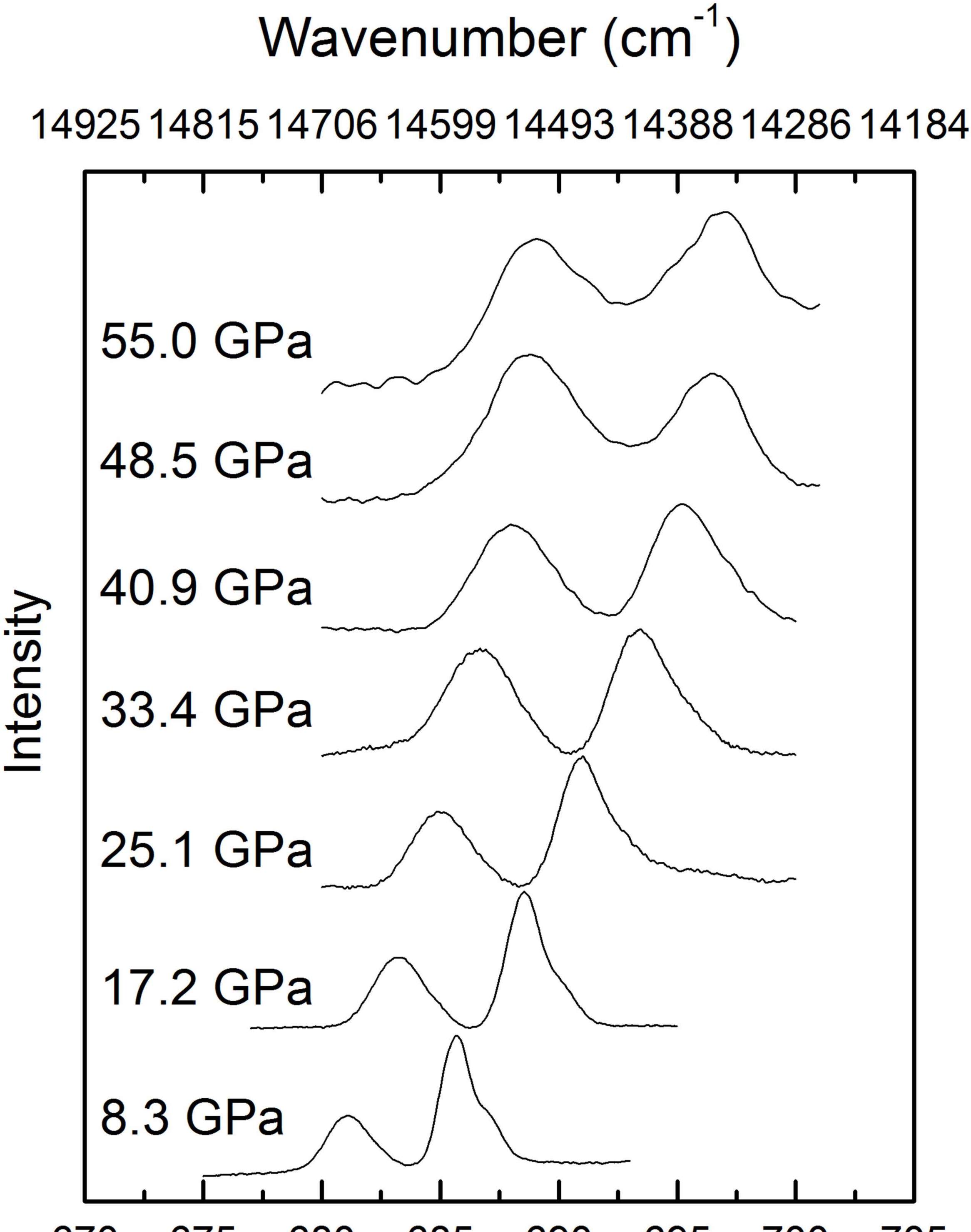
Wavenumber (cm-1)
14925 14815 14706 14599 14493 14388 14286 14184
55.0 GPa
48.5 GPa
40.9 GPa
33.4 GPa
25.1 GPa
17.2 GPa
8.3 GPa
Intensity
670 675 680 685 690 695 700 705
Wavelength (nm)

Figure 4

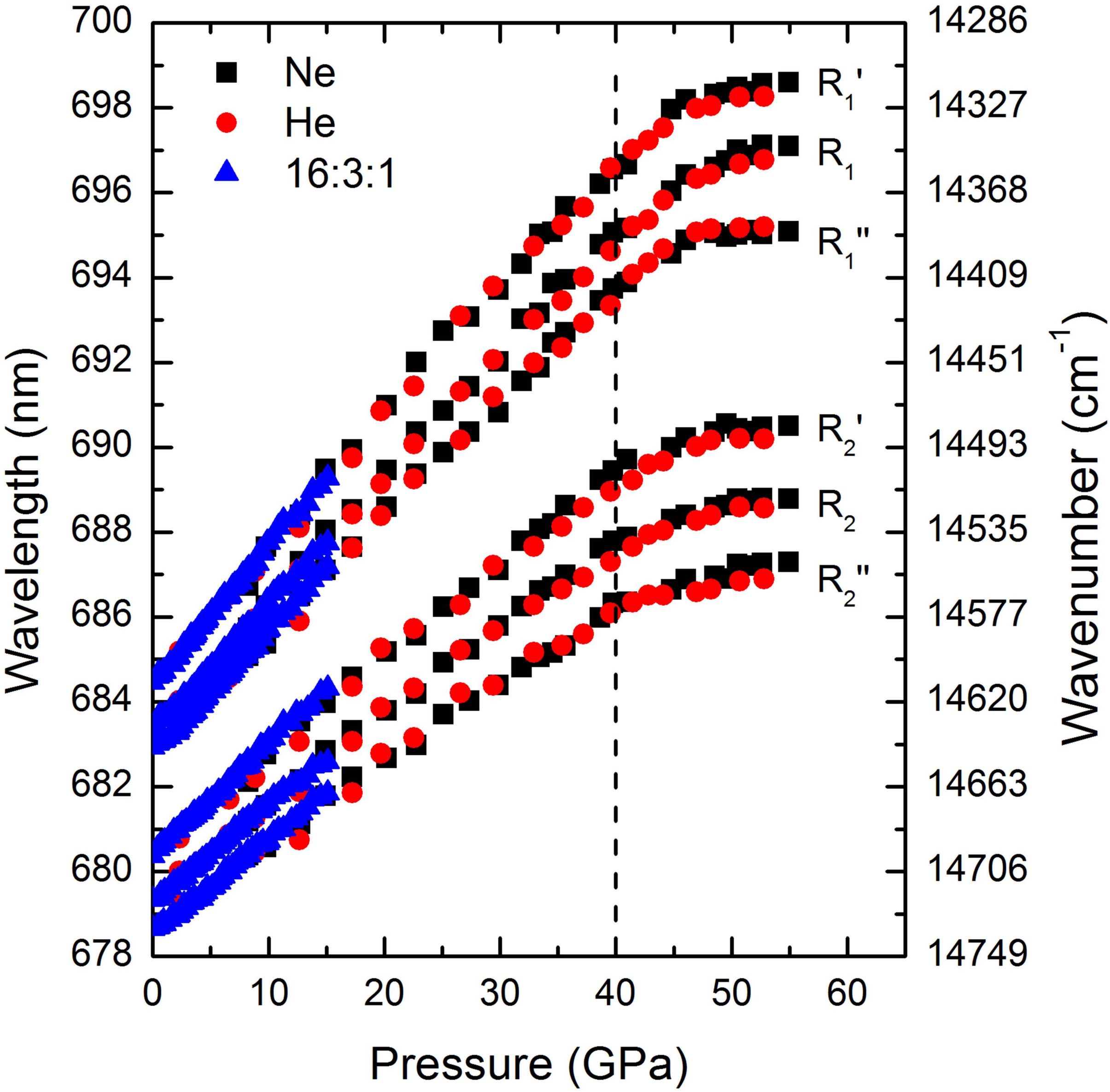
Ne
He
16:3:1
R1'
R1
R1''
R2'
R2
R2''
Wavelength (nm)
Wavenumber (cm-1)
Pressure (GPa)
700
698
696
694
692
690
688
686
684
682
680
678
14286
14327
14368
14409
14451
14493
14535
14577
14620
14663
14706
14749
0
10
20
30
40
50
60

Figure 5

a

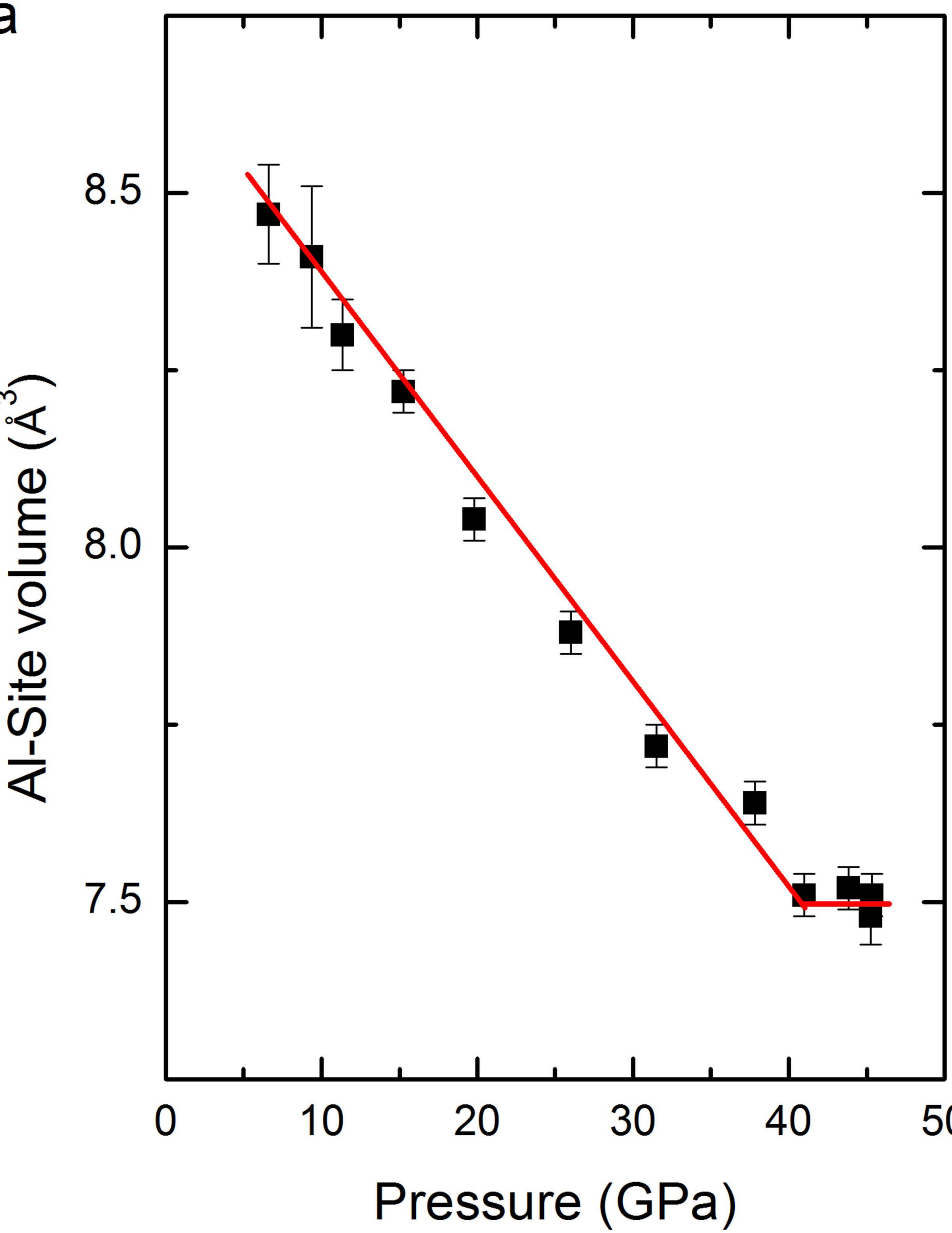

Figure 6a

b

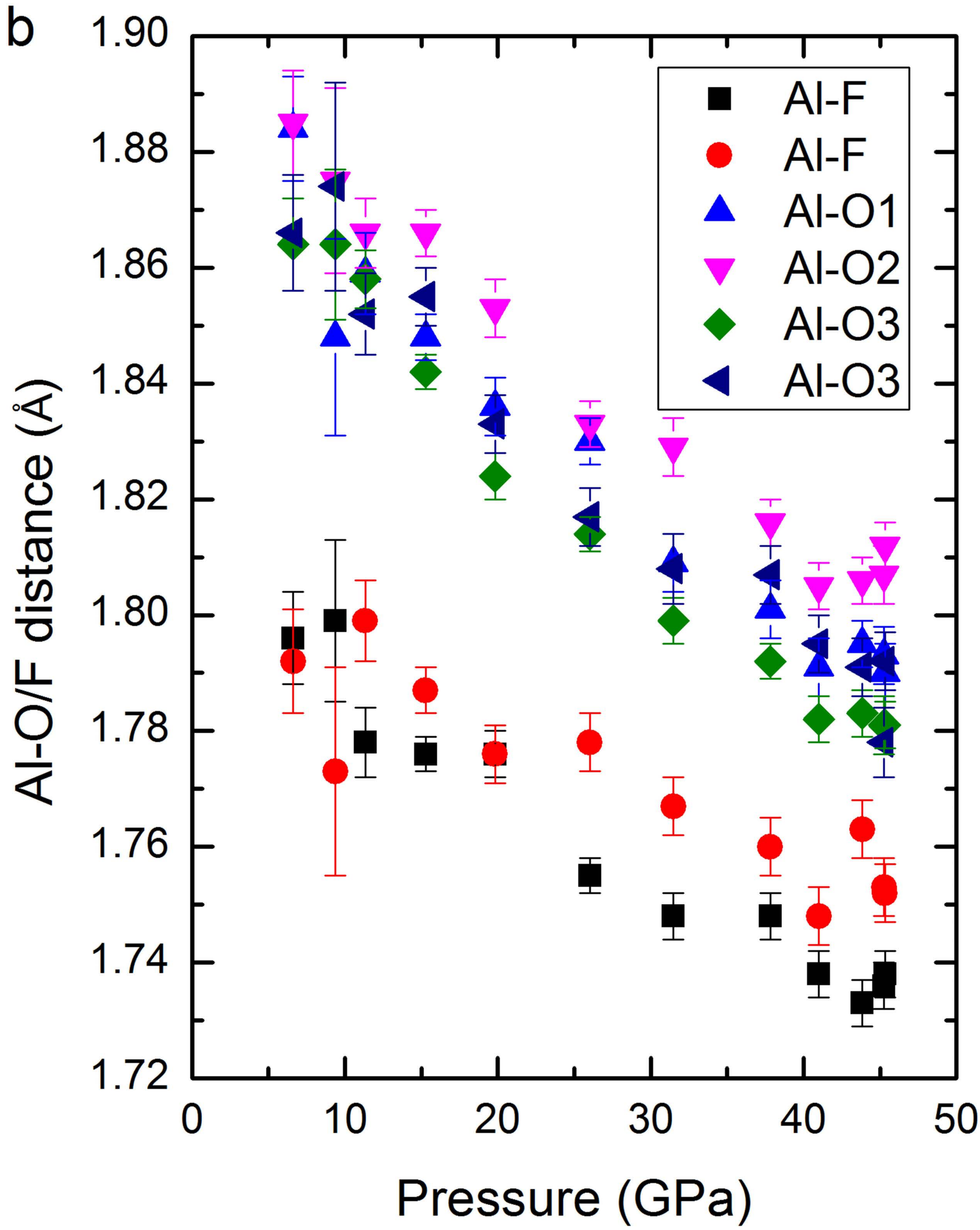
Al-F
Al-F
Al-O1
Al-O2
Al-O3
Al-O3
Al-O/F distance (Å)
1.90
1.88
1.86
1.84
1.82
1.80
1.78
1.76
1.74
1.72
0
10
20
30
40
50
Pressure (GPa)

Figure 6b

a

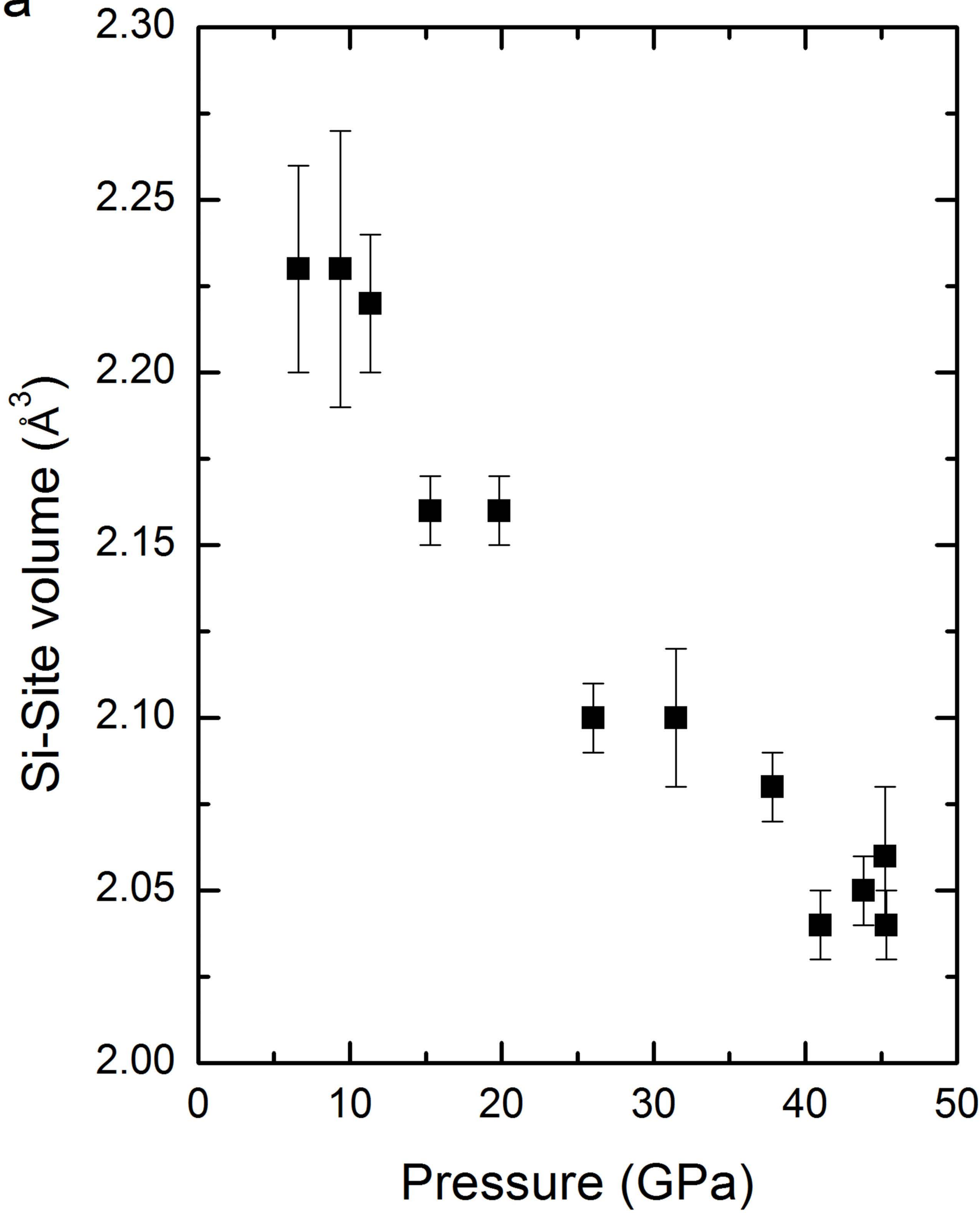
2.30
2.25
2.20
2.15
2.10
2.05
2.00
Si-Site volume (Å3)
0
10
20
30
40
50
Pressure (GPa)

Figure 7a

b

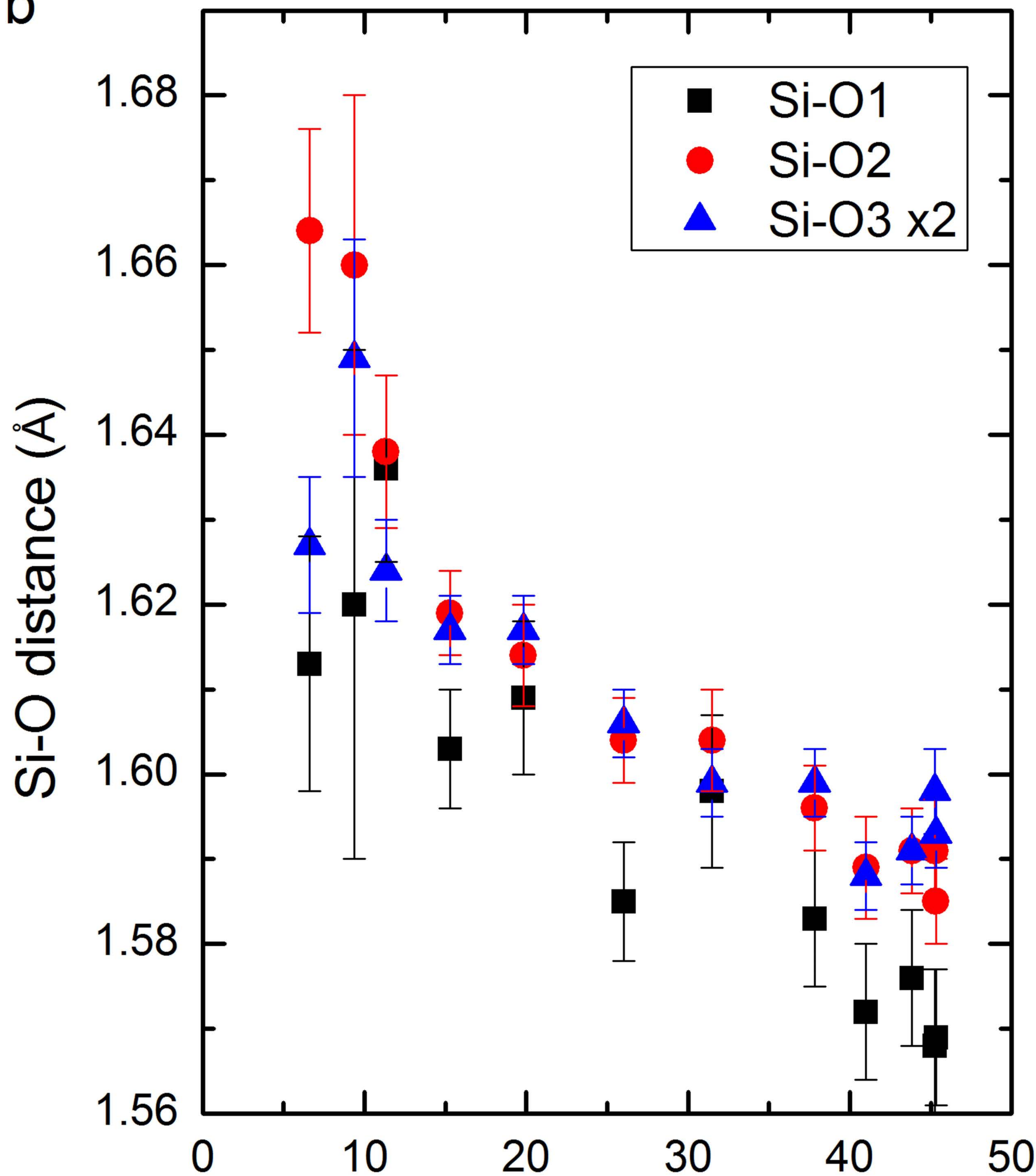
Si-O1
Si-O2
Si-O3 x2
Si-O distance (Å)
1.68
1.66
1.64
1.62
1.60
1.58
1.56
0
10
20
30
40
50
Pressure (GPa)

Figure 7b

a

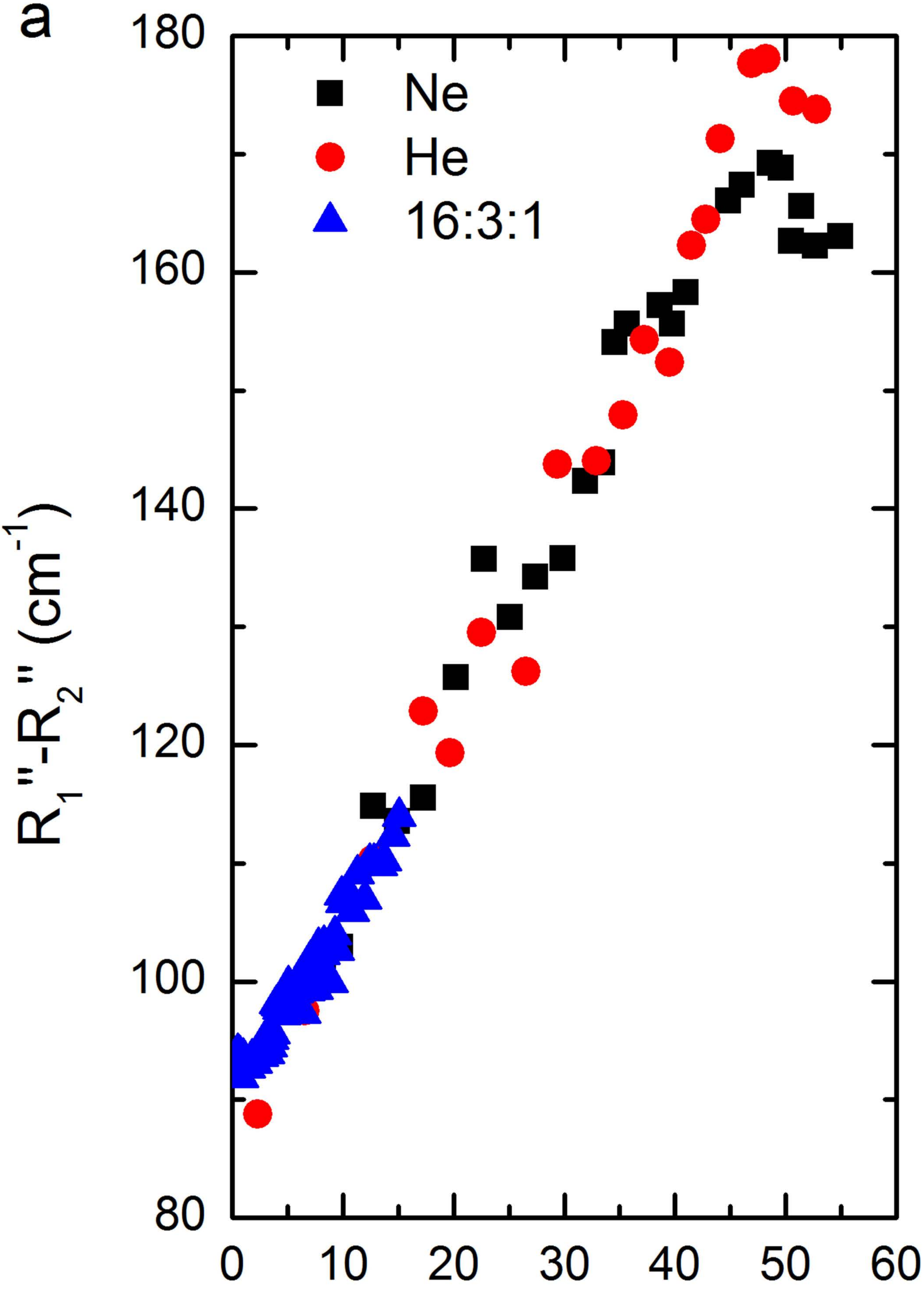
Ne
He
16:3:1
180
160
140
120
100
80
R_1''-R_2'' (cm^{-1})
0
10
20
30
40
50
60
Pressure (GPa)

Figure 8a

b

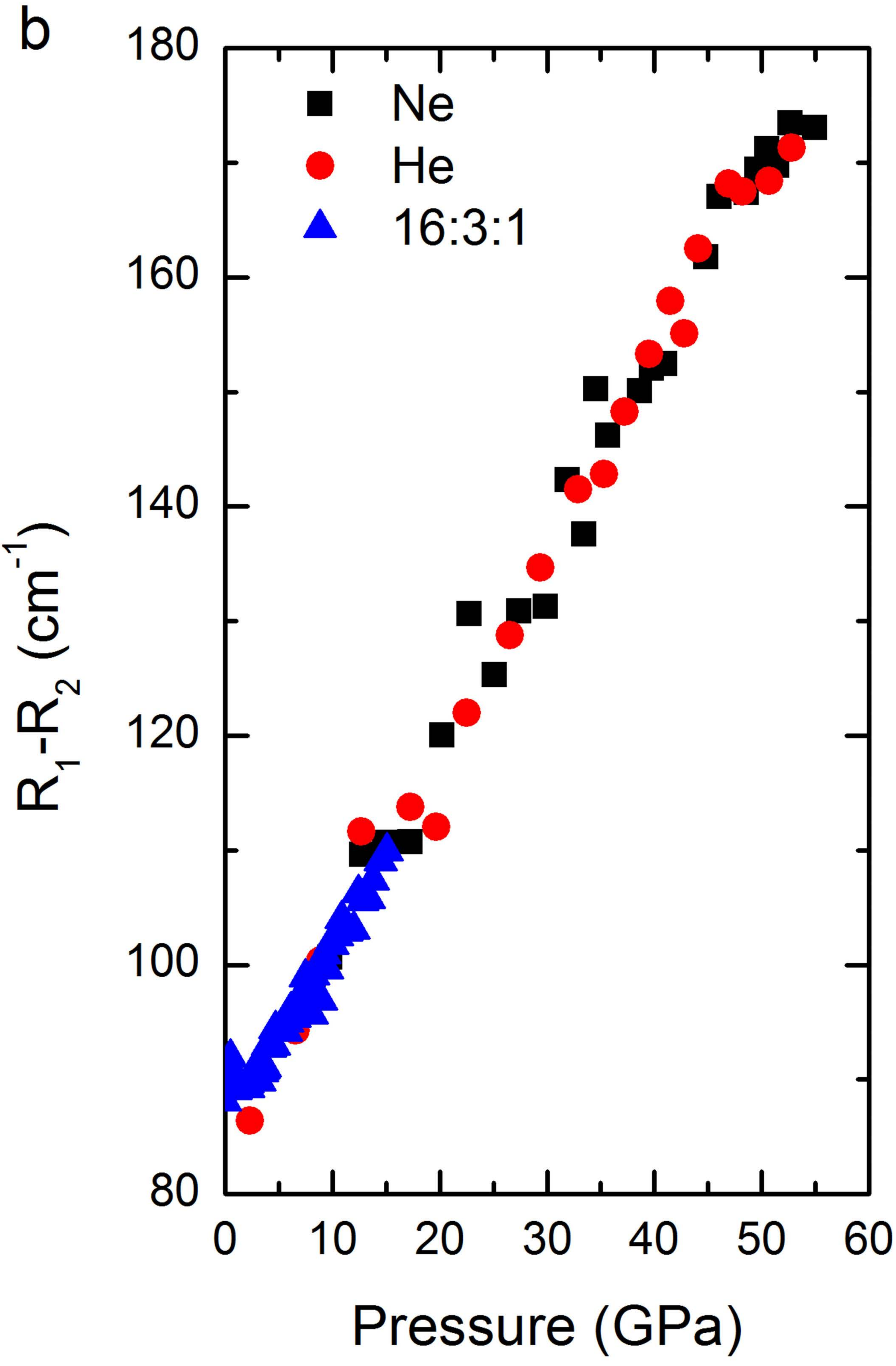
Ne
He
16:3:1
180
160
140
120
100
80
R_1-R_2 (cm^{-1})
0
10
20
30
40
50
60
Pressure (GPa)

Figure 8b

C

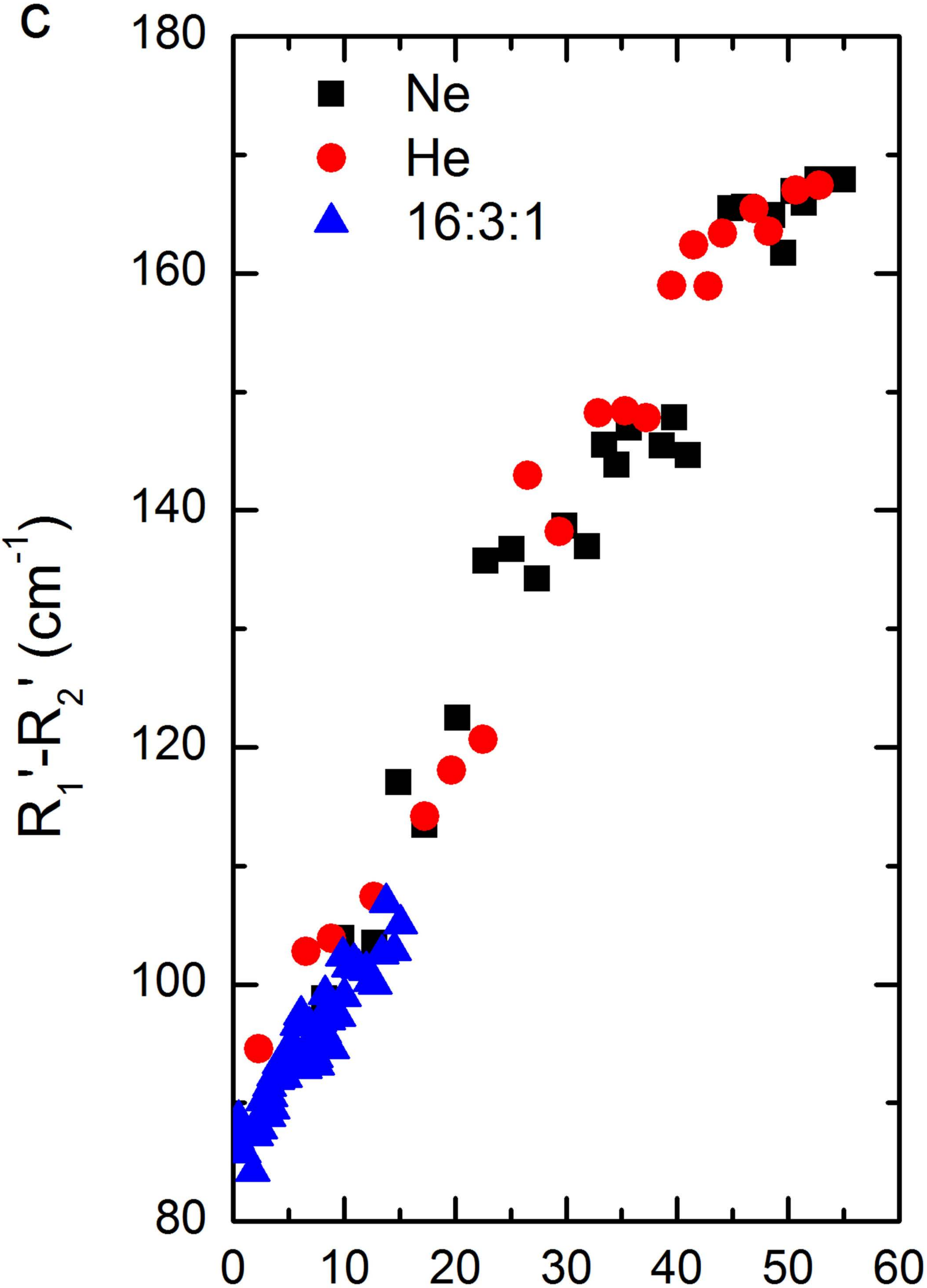
Ne
He
16:3:1
180
160
140
120
100
80
R_1'-R_2' (cm^{-1})
0
10
20
30
40
50
60
Pressure (GPa)

Figure 8c

a

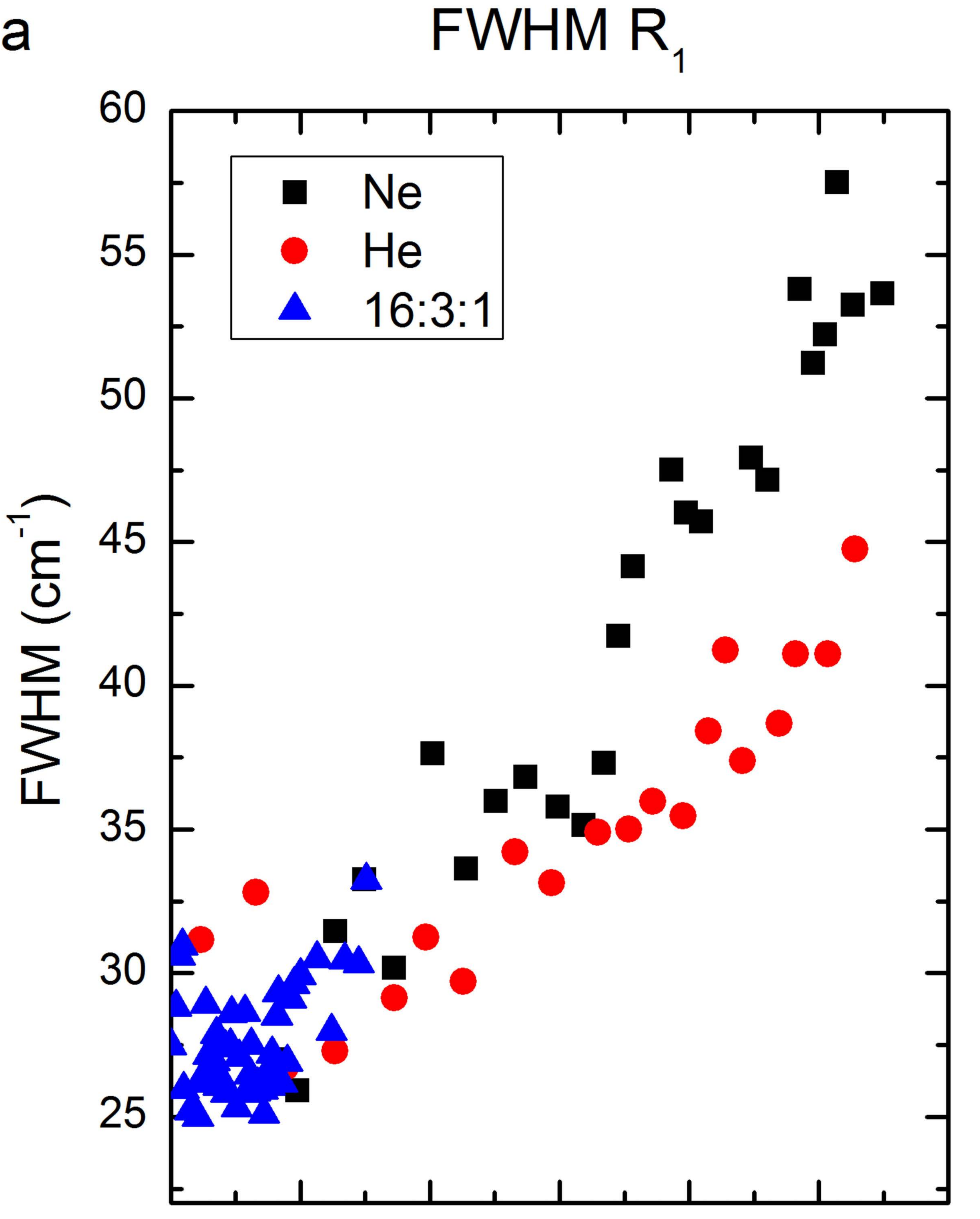
FWHM R1
Ne
He
16:3:1
FWHM (cm-1)
60
55
50
45
40
35
30
25
0
10
20
30
40
50
60
Pressure (GPa)

Figure 9a

b

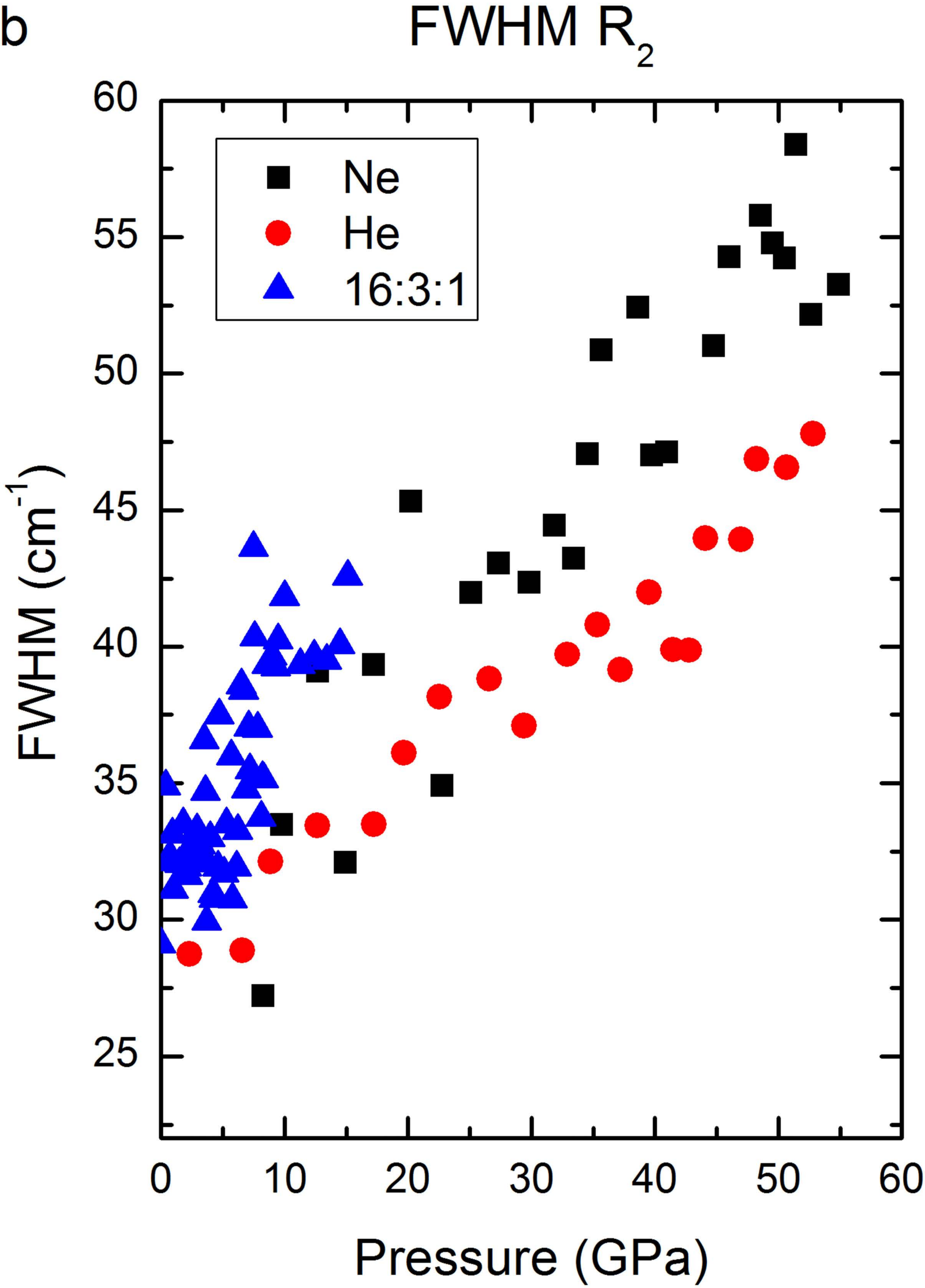
FWHM R2
Ne
He
16:3:1
FWHM (cm-1)
Pressure (GPa)
60
55
50
45
40
35
30
25
0
10
20
30
40
50
60

Figure 9b